Eur. Phys. J. AP **7**, 45–57 (1999)

THE EUROPEAN PHYSICAL JOURNAL APPLIED PHYSICS

Computation of 3D curvatures on a wet snow sample

J.B. Brzoska[1,a], B. Lesaffre[1,b], C. Coléou[1,c], K. Xu[2,d], and R.A. Pieritz[3,e]

[1] Météo-France, CNRM/Centre d'Études de la Neige, 1441 rue de la Piscine, 38406 St Martin d'Hères, France
[2] Laboratoire de Physique des phénomènes de Transport et de Mélange, Bd3, Téléport2, B.P. 79, 86960 Futuroscope, France
[3] Laboratoire d'Études des Transferts en Hydrologie et Environnement, B.P. 53, 38041 Grenoble Cedex 9, France

Received: 8 October 1998 / Revised: 15 April 1999

Abstract. The map of 3D curvatures of a porous medium characterizes most of its capillary properties. A model for directly computing curvatures from a three-dimensional image of the solid matrix of a porous medium is presented. A precise distance map of the object is built using the "chamfer" distance of discrete geometry. The set of local maxima of the distance map is used for quick location of the normal to each point P of the object's surface. The normal being known, principal radii of curvature are computed in 2D and lead to 3D curvature. This model was validated on geometric shapes of known curvature, then applied on a natural snow sample. The snow image was obtained from a serial cut (performed in cold laboratory) observed under specularly reflected light. Views of both fresh and sublimated sections were taken for each of the 64 section planes: this allowed easier distinction between snow and filling medium and made possible automatic contouring of section plane images. Curvature maps computed from pore and grain phases respectively were found to be in excellent agreement for each tested object shape, including the snow sample.

PACS. 92.40.Rm Snow – 07.05.Pj Image processing – 61.43.Gt Powders, porous materials

Introduction

Capillarity in a porous medium is governed by the 3D map of solid matrix curvatures [1]. Curvature is a fully three-dimensional parameter, difficult to derive from 2D data such as section planes. Its computation requires a fine description of the grain's shape *i.e.* high resolution 3D imaging.

Curvature has long been recognized as a central parameter in snow microphysics [2]. Its importance derives from the fact that the pore size distribution of snow clusters in the capillary range (0.1- 1 mm). The structure of snow evolves with temperature and humidity fields; the effect of the presence of liquid water is specially strong when the temperature reaches 0 °C. Except at the high sublimation rates leading to faceted shapes, these structure modifications are governed by local curvature.

Until recently, only the 2D local curvature of grains could be used. This gave valuable information on grain types for modeling snow metamorphism but could not, for instance, correctly account for water percolation. This paper presents a numerical method for modeling 3D local curvatures, followed by an original experimental validation on snow.

The principle of the model is first to compute a "skeleton" of the 3D image of the sample (image processing technique); these skeleton data are then used to locate the normal vector $\mathbf{n}$ at any point of the grain phase edge. The knowledge of $\mathbf{n}$ allows the derivation of principal planes (and radii R_1 and R_2) of curvature in 2D, and then 3D local curvature $C = (1/2)(1/R_1 + 1/R_2)$. After a description of the fast algorithm used to compute this skeleton, the procedure of 2D computation is presented.

The next section deals with the details of experimental 3D file generation. The experiment which aimed at providing a set of serial section planes of snow is first presented. The image processing used to obtain an isotropic 3D binary data file is then thoroughly described. The last section presents validations of the model. Using digitized geometrical shapes whose curvature map is analytically known, allowed first debugging, then numerical and digitization errors to be assessed. Results on data from the wet snow sample are then presented and compared to standard 2D computations on grain outlines, showing the good agreement of these two approaches.

Finally, the problem of resolution *vs.* field size is summarized: our choice of parameters seems to be adapted to wet snow, but will have to be considered again for other snows or materials. Outlook and conclusions of this work

[a] e-mail: jean-bruno.brzoska@meteo.fr
[b] e-mail: bernard.lesaffre@meteo.fr
[c] e-mail: cecile.coleou@meteo.fr
[d] Study performed at Centre d'Étude de la Neige.
[e] e-mail: rap@hmg.inpg.fr

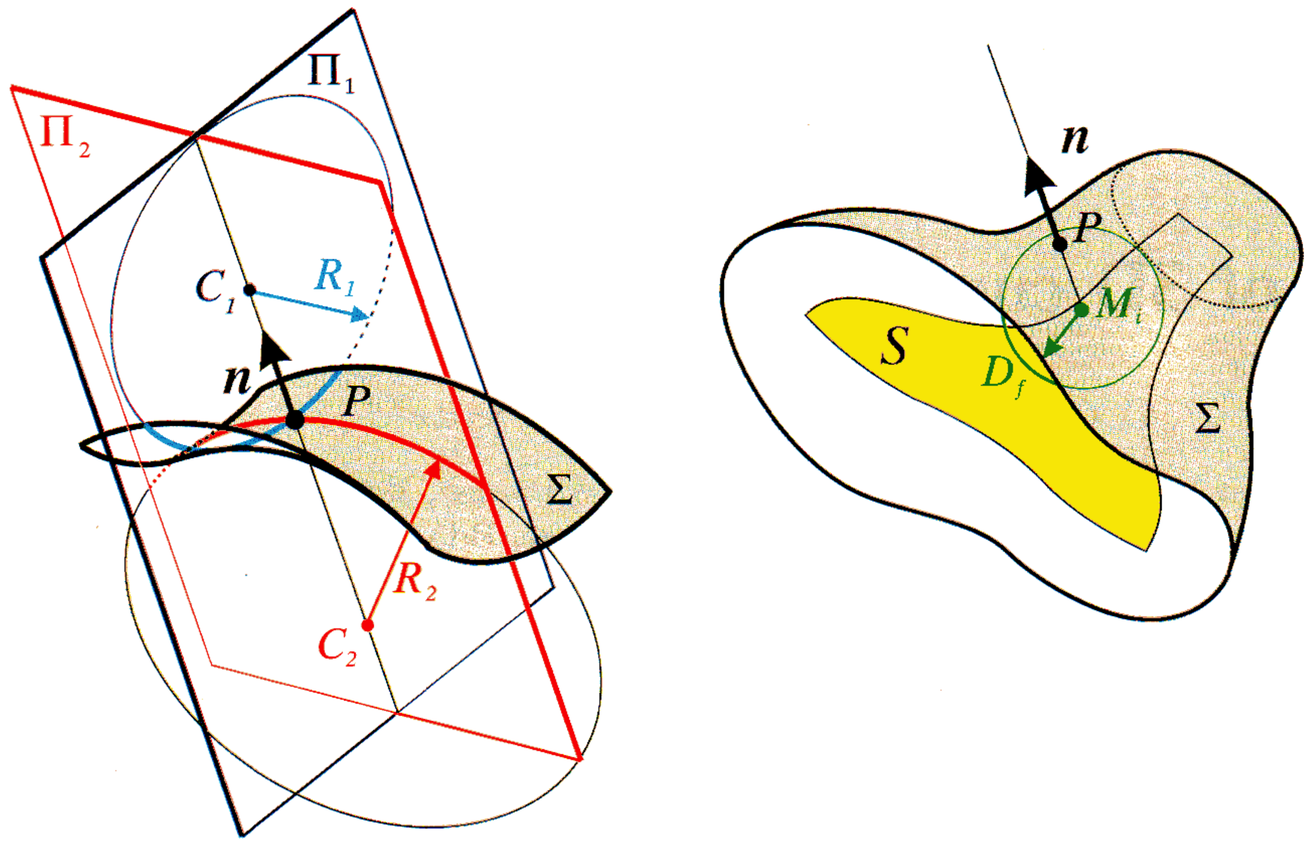

Fig. 1. *Left* – principal radii of curvature R_1 and R_2: $C = (1/2)(1/R_1 + 1/R_2)$; Π_1 and Π_2: principal planes; C_1 and C_2: curvature centers; P: current point; Σ: surface of the 3D object O; $\mathbf{n}$: normal vector; Π_1 is orthogonal to Π_2; Π_1 and Π_2 both contain $\mathbf{n}$. *Right* – location of $\mathbf{n}$ using the skeleton (medial axis) S; M_i: current point of the skeleton; D_f: background (chamfer) distance associated to M_i; the sphere of center M_i and radius D_f meets Σ at a point P so that $\mathbf{PM}_i$ is colinear to $\mathbf{n}$.

stress "remote" 3D imaging techniques which we consider to be the future for snow microstructure studies.

1 Model

1.1 Geometrical fundamentals of the model

Three-dimensional (local) curvature C can be obtained on every point P of the surface Σ of an object O from the principal radii of curvature ρ_1 and ρ_2 (mathematically the largest and the smallest one) at P

$$C = \frac{1}{2}\left(\frac{1}{\rho_1} + \frac{1}{\rho_2}\right).$$

Practically, any couple of values R_1 and R_2 for which the curvature planes Π_1 and Π_2 are orthogonal with the other and contain the normal vector $\mathbf{n}$ can be used as principal radii of curvature [3]: they fulfill indeed the condition $C = (1/2)(1/R_1 + 1/R_2)$. This meaning of "principal radii of curvature" will be used in the following. Whereas several algorithms are known to compute two-dimensional radii of curvatures [4], it is still difficult to quickly locate a normal vector $\mathbf{n}$ with sufficient accuracy.

The main idea of our model is to use a medial axis of the object to locate $\mathbf{n}$ easily in order to compute R_1 and R_2 (the concept of medial axis comes from imaging techniques, see Serra [5]). The normal $\mathbf{n}$ being located, two orthogonal planes Π_1 and Π_2 containing $\mathbf{n}$ are computed. The intersection of Σ with each of these planes is a plane curve, from which the 2D radii of curvature are computed, giving $C(P)$: these 2D computations use little memory since each point is processed separately and requires only its closest neighbors.

A non-connected medial axis is used to locate $\mathbf{n}$. It is the set of centers of the largest spheres tangent to the object surface Σ [4], which generally appears as a skew surface (like ribbons) "at the middle" of O. On parts of O whose cross-section is circular, the medial axis is simply a curve.

1.2 Chamfer algorithm and medial axis determination

For a given numerical object O, the background distance d_b of a point P belonging to O is defined as:

$$\forall (P \in O, Q \notin O), \quad d_\mathrm{b} = \min[d(P,Q)].$$

The map of background distances can be built using a two-run iterative procedure [4]. The first run starts from the corner of zero indices of the digitized space and processes voxels one by one towards increasing indices. When a given voxel P is "reached" by the procedure, its lowest discrete distance d_f to object's edge voxels which were already processed is computed as:

$$d_\mathrm{f}(P) = \min_{\{N(P)\}} \Big[d_\mathrm{f}[N(P)] + d[P, N(P)] \Big]$$

where $N(P)$ denotes a given *already processed* (in this run, lower indices) neighbour of P and d the distance used in the digitized space; this value is assigned to P. This forward run ends at the opposite space corner (maximum indices).

The same procedure is then applied *backwards* from the high indices corner, toward decreasing indices, taking into account results of the forward run: to a given voxel

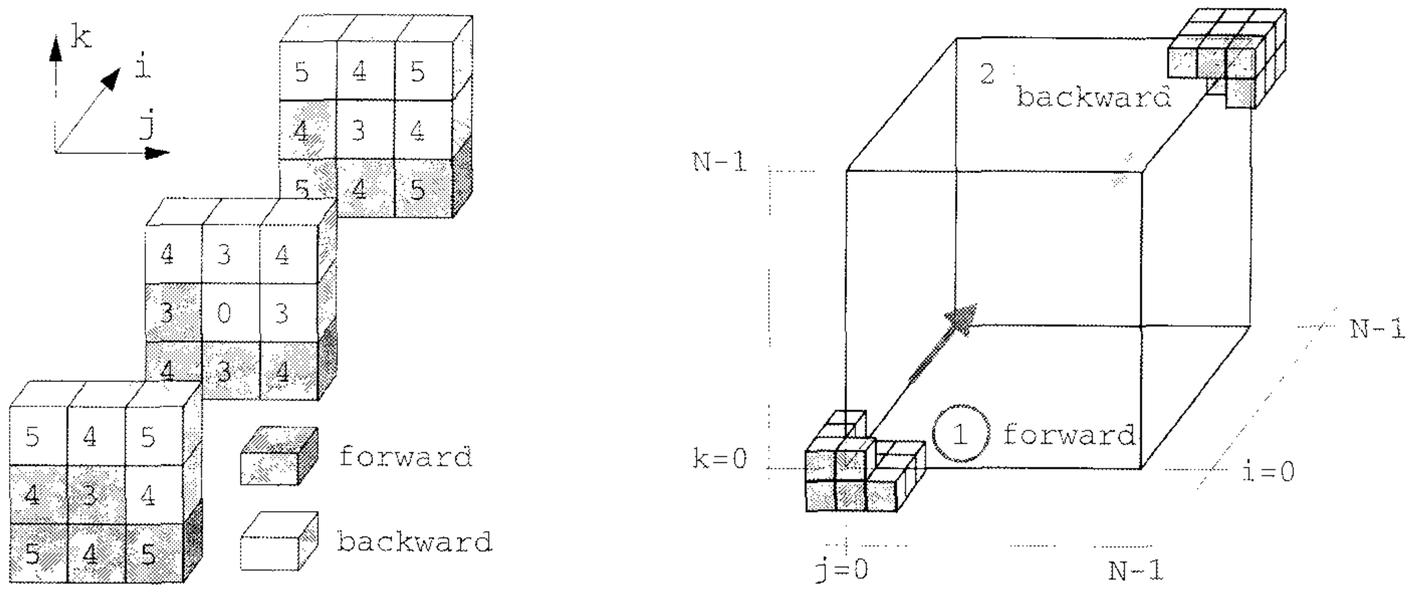

Fig. 2. Algorithm for chamfer distance d_{345} computation. *Left* the two half-kernels. Note that the current point (the center of the whole kernel) is taken into account only in the "backward" run. *Right* – propagation of each half-kernel across the image. Forward run: increasing indices (i then j then k) from 0 to $N-1$ (N is the resolution: in this study, $N = 128$). Backward run: decreasing indices (i then j then k) from $N-1$ to 0.

P reached by the backward run is assigned the value:

$$d_{\mathrm{b}}(P) = \min\left[d_{\mathrm{f}}(P),\ \min_{\{N(P)\}}\left[d_{\mathrm{b}}[N(P)] + d[P, N(P)]\right]\right]$$

d_{b}, the minimal distance of P to edge voxels toward two opposite directions (respectively maximum and zero indices corners), is the desired background distance of P indeed.

The discrete distance used in the algorithm is the so-called "chamfer distance" d_{345}, equal to unity along Euclidean axes, 4/3 along the small diagonal (instead of the Euclidean value of $\sqrt{2}$) and 5/3 along the large diagonal (instead of $\sqrt{3}$). The unit ball of d_{345} (shown in Fig. 3a) fits correctly the Euclidean unit sphere in any direction (better than within $\pm 5\%$ in radius), which limits digitization errors. Moreover, this distance allows to save memory because it uses integers.

The (unconnected) medial axis has been defined as the set of voxels whose background distance d_{b} is a local maximum with regard to neighboring voxels:

$$P \in S \Leftrightarrow \forall N \in \{N(P)\},\quad d_{\mathrm{b}}(P) \geq d_{\mathrm{b}}[N(P)].$$

This simple definition of a skeleton does not preserve connectivity, but allows the full reconstruction of the object (within the limits of the chosen discrete distance): any voxel of the object's surface can be related to a voxel of S and its curvature can then be computed.

1.3 From medial axis to curvatures

By construction, M_S being a point of the medial axis S and $d_{\mathrm{b}}(M_S)$ the background distance of M_S (already computed), the intersection between the edge Σ of the object O and the sphere of center M_S and radius $d_{\mathrm{b}}(M_S)$ is a set of points $\{P(M_S)\}$ so that for each $P(M_S)$, $\mathbf{P}(\mathbf{M}_S)\mathbf{M}_S$ is theoretically parallel to $\mathbf{n}$.

Numerically, many points of Σ can be found each being related to several points M_S of S – *not always close together*, whereas some other points of Σ remain "untouched" by points of S. This can lead to missing points (if $\mathbf{n}$ is undefined, C cannot be computed), and also to wrong values of C for the points of Σ reached by spheres from several points of S (they are many). This is due to digitization and to the fact that whereas the coordinates of the voxels of O are naturally Euclidean (and cannot easily be anything else), the chamfer distance is not (the unit ball for d_{345} is not a Euclidean sphere, see Fig. 3a).

To optimize the location of $\mathbf{n}$, the closest voxel of S (with regard to the chamfer distance) is related to the current voxel of Σ. for each voxel of Σ (this "optimal" procedure requires a long CPU time). A list containing the coordinates of each voxel P_S of Σ, its associated unique voxel M_S of S, and then the corresponding distance d_{b} is provided.

$\mathbf{n}$ being known for each voxel of Σ, principal planes Π_1 and Π_2 can then be computed; they must be orthogonal together and contain $\mathbf{n}$. The first one is arbitrarily chosen to contain one of the three axes of coordinates. Then the intersection of each of these planes with the digitized object should be derived (see Fig. 3b).

The plane is first assigned a square grid with the same size as the original cubic grid of the 3D image. Π_1 and Π_2 are digitized and defined in a neighbourhood of P large enough to compute correctly 2D curvatures (in our case, a 20×20 pixels square centered on P, in the 2D frame of the considered plane). Then the coordinates of the centers of their pixels in the original 3D frame of the image are computed. If they fall inside "object" voxels of O (assigned to 1), the corresponding pixels in the considered principal plane are also assigned to 1 (else zero). The resulting set of points of Π_1 (respectively Π_2) is a new 2D image of the intersection of O and Π_1 (respectively Π_2). An additional digitization error comes from the arbitrary orientation of the 2D grids of principal planes with regard to the 3D image cubic grid. It is comparable to the error due to the digitization of the original 3D object.

Then radii of curvature (2D) are computed by means of parabolic interpolation of grain contours [8]. The accuracy of parabolic interpolation depends on the number

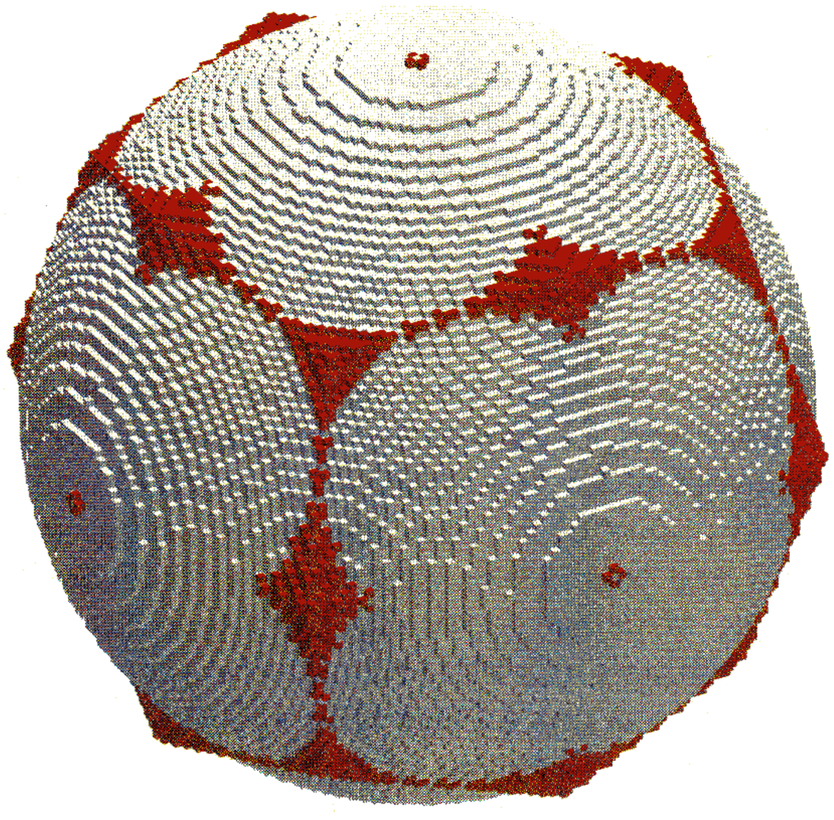

(a)

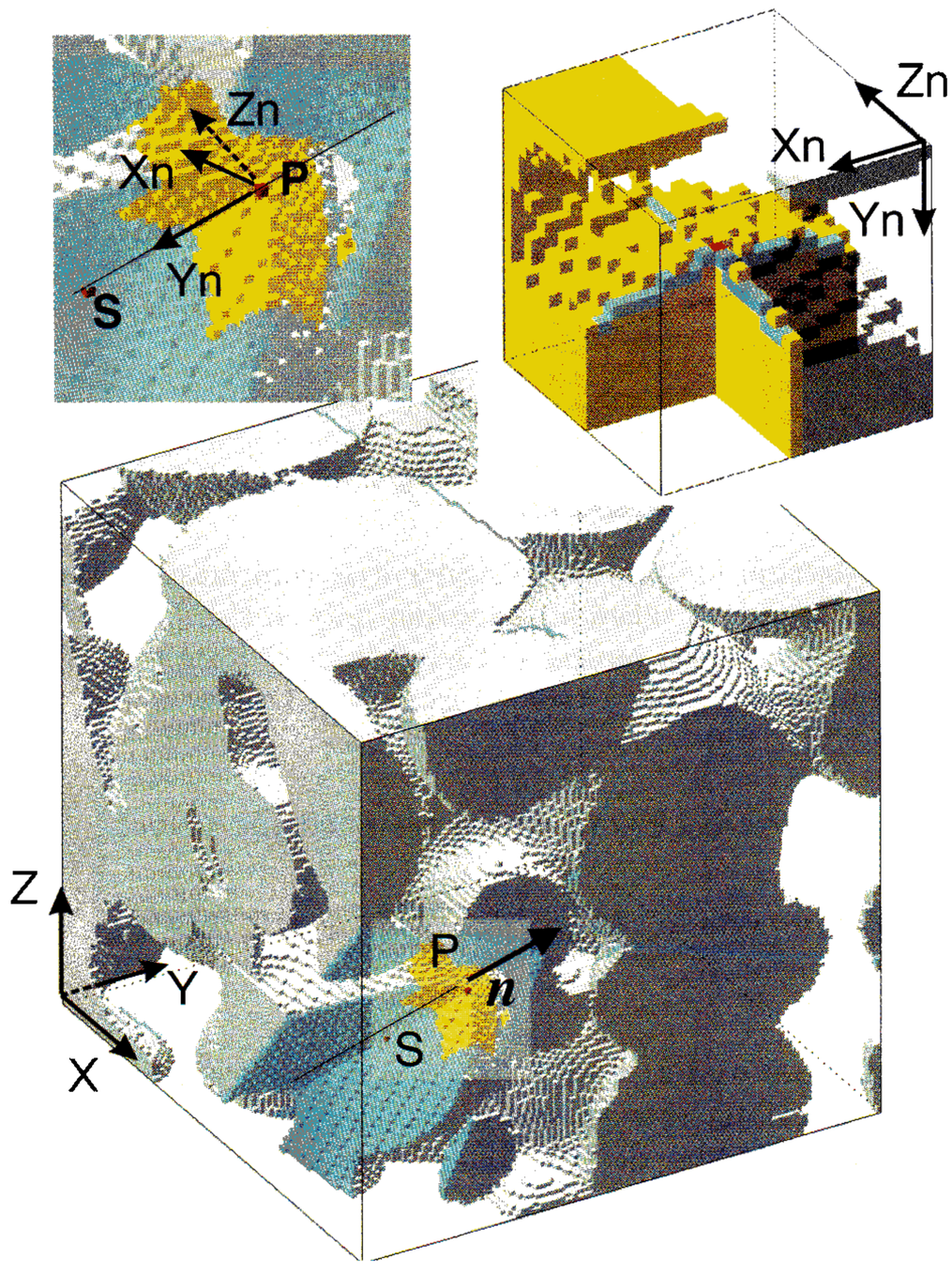

(b)

Fig. 3. (a) Chamfer distance d_{345} *vs.* Euclidean distance. The ball for d_{345} (red) overestimates the sphere size (Euclidean ball, grey) in the direction of first neighbors, whereas its mean radius is slightly smaller than the sphere radius. (b) From normal vector **n** to 2D curvature computations: XYZ frame of the original 3D image, $X_nY_nZ_n$ – local frame related to the current point P (red), $\mathbf{Y}_n$ colinear to **n**. S denotes here the point of the skeleton related to P. *Left detail*: PY_nZ_n contains vectors **n** and **X**: plane Π_1, PX_nY_n contains **n** and is orthogonal to Π_1: plane Π_2. The yellow region denotes the voxels in the object which belong to the working neighborhood of P, $WN(P)$. *Right detail*: $WN(P)$ is defined (and drawn here) in the local frame $X_nY_nZ_n$. P is drawn at its center in red. Principal radii of curvature R_1 and R_2 are actually computed on the two arcs appearing in blue. The front part of $WN(P)$ is drawn in grey transparency color for a complete visibility of arcs.

of neighbouring pixels on both sides of the current pixel. If less than 4 neighbouring pixels are available, the calculation is not performed .

2 Experiments and image processing

Our intention was to apply the model to a 3D file of a real, non-reconstructed porous medium. Moreover, the resolution of this data file should be high enough to account for grain shape, bond geometry or capillarity. We decided to realize such a data file from a refrozen wet snow sample.

2.1 Sample preparation

Wet snow samples were prepared in our cold laboratory [9], in an isothermal box held at 0 °C (double walls filled with an ice-water mixture). Natural snow (sampled in the field, then stored at −20 °C) was sieved into the box. Water at 0 °C was poured by the bottom of the box (by decanting), then removed in the same way at the end of the soaking period. This ensured that each part of a given horizontal plane of the snow block had been in contact with water during the same time. Since wet grain snow presents large pores, hydrostatic equilibrium was reached in a few second and therefore, the procedure could be assumed to be quasistatic.

Measurement samples (cores) were taken at the center of this wet snow block; inner parts of the sample were given an extra protection (thermal and hygrometric) by the external layers of this same sample. At least two adjacent cores were taken in the same horizontal plane; they were processed immediately. The first one was used for determination of liquid water content (LWC) by cold calorimetry [10], the other(s) was (were) prepared for serial cut experiments. At the same moment, a few grain clusters were taken from the inner part of the block and dipped

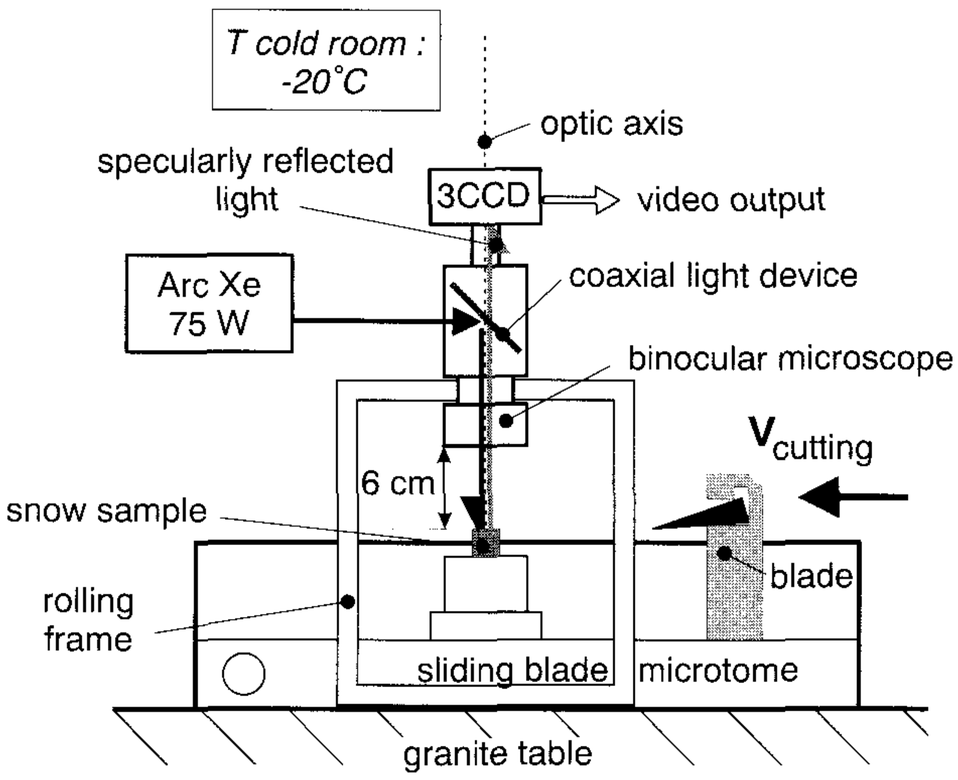

Fig. 4. Experimental device for serial cuts.

into isooctane for preservation [11]. The day after, images of their outline (contour of their projection onto the focal plane of the microscope) were recorded under transmitted light. Then the histogram of 2D curvature of outlines was computed [8] for further comparison with 3D curvatures.

2.2 Serial cuts

For this experiment, the "fresh" sample was first frozen naturally in the cold laboratory (1 hour at -5 °C). The frozen sample was soaked by decanting ethyl orthophtalate at -4 °C (phtalate for short, m.p. -5 °C), then the cold laboratory was set to -20 °C till the end of the experiment. After freezing the whole (6 hours at -20 °C), a slice 1 cm thick was sawed from the frozen core and mounted onto a sliding blade microtome (Leica histoslide 2000).

Video views were taken through a binocular microscope, straight over the section plane of the microtome (see Fig. 4), using the specularly reflected light produced by a coaxial lighting device (metallographic technique). At low magnification, the microscope has a large frontal distance (more than 30 mm): we could run the blade (working at a constant altitude in our model of microtome) without needing to change focus. It was then possible to perform all the serial cut regularly.

Once a section plane was made, two views were taken successively (see Fig. 5), 3 s after cutting (snow grains presented the characteristic "dull" surface of freshly cut ice), and 30 s later (because of sublimation, the ice surface presented a brighter surface with visible dots, whereas phtalate surfaces remained unchanged). Such pairs of images provided a valuable "thermodynamic filtering" for a further automatic edge detection. Neglecting undesired sample displacements, only the aspect of the ice phase changed from one view to another.

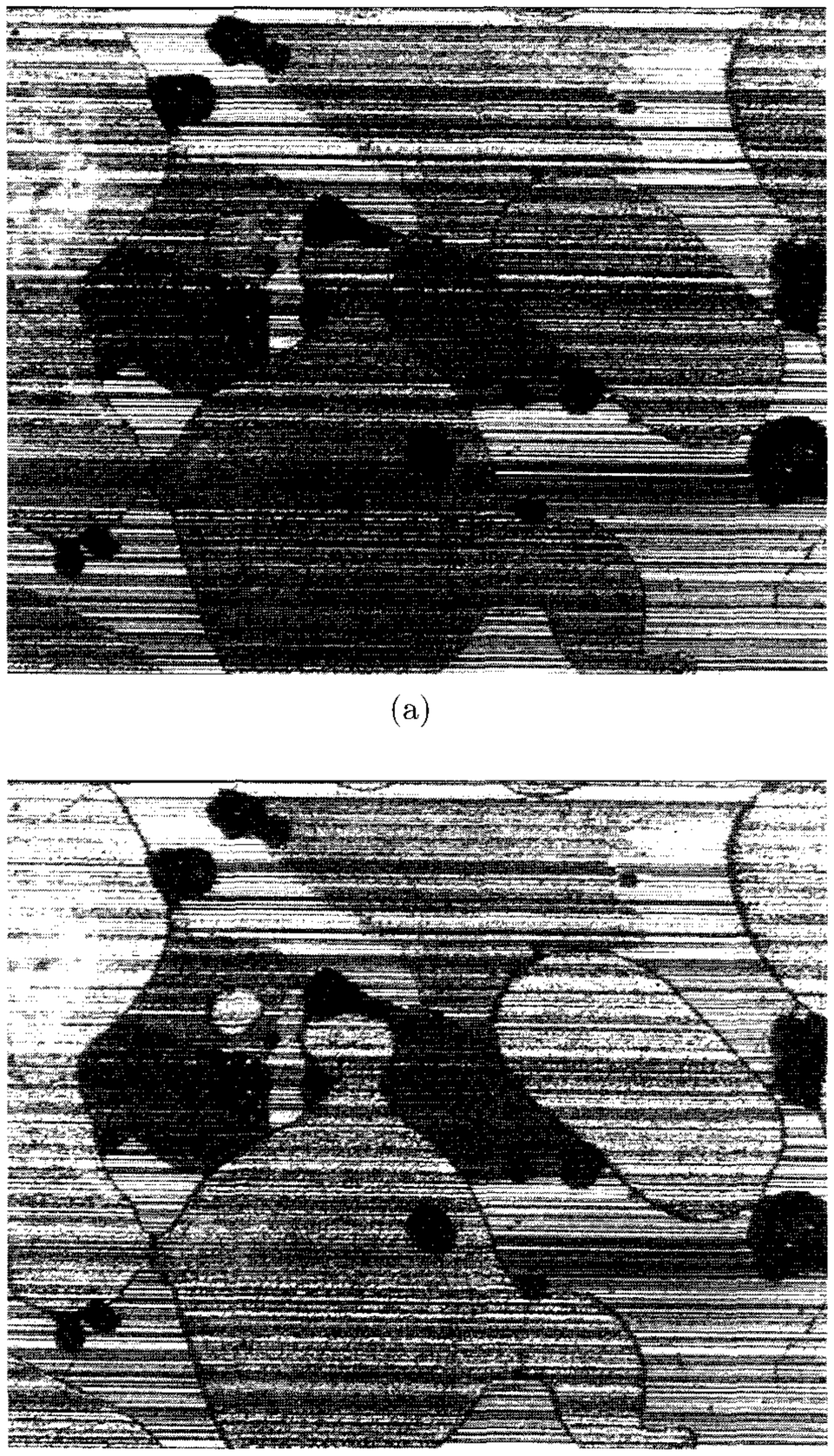

(a)

(b)

Fig. 5. Raw images of section planes under reflected light. Resolution 768×576 pixels. Pixel size: 5 μm. (a) "Fresh" section (3 s after cutting). (b) Sublimated section (30 s later, in the cold room at $T = -20$ °C, $T_d \approx -30$ °C).

2.3 3D data file generation

64 section planes were obtained by working our experimental device for $\sim$ 2 hours in the cold laboratory at -20 °C. Two views were taken from each section plane, which provided 2 sets of 64 images. Each image was made of 512×512 pixels 5 μm wide; the vertical spacing between two successive section planes was 40 μm. For the set of "sublimated" images, each grey-level image was then contoured manually to produce binary images (total processing time: 2 weeks). The resolution with respect to xy (5 μm) was much higher than with respect to z (40 μm). Moreover, grain size (of the order of millimeter) is large as compared to the cutting increment of 40 μm. We have therefore decided to interpolate one section plane out of two in order to provide a binary file of 128^3 voxels,

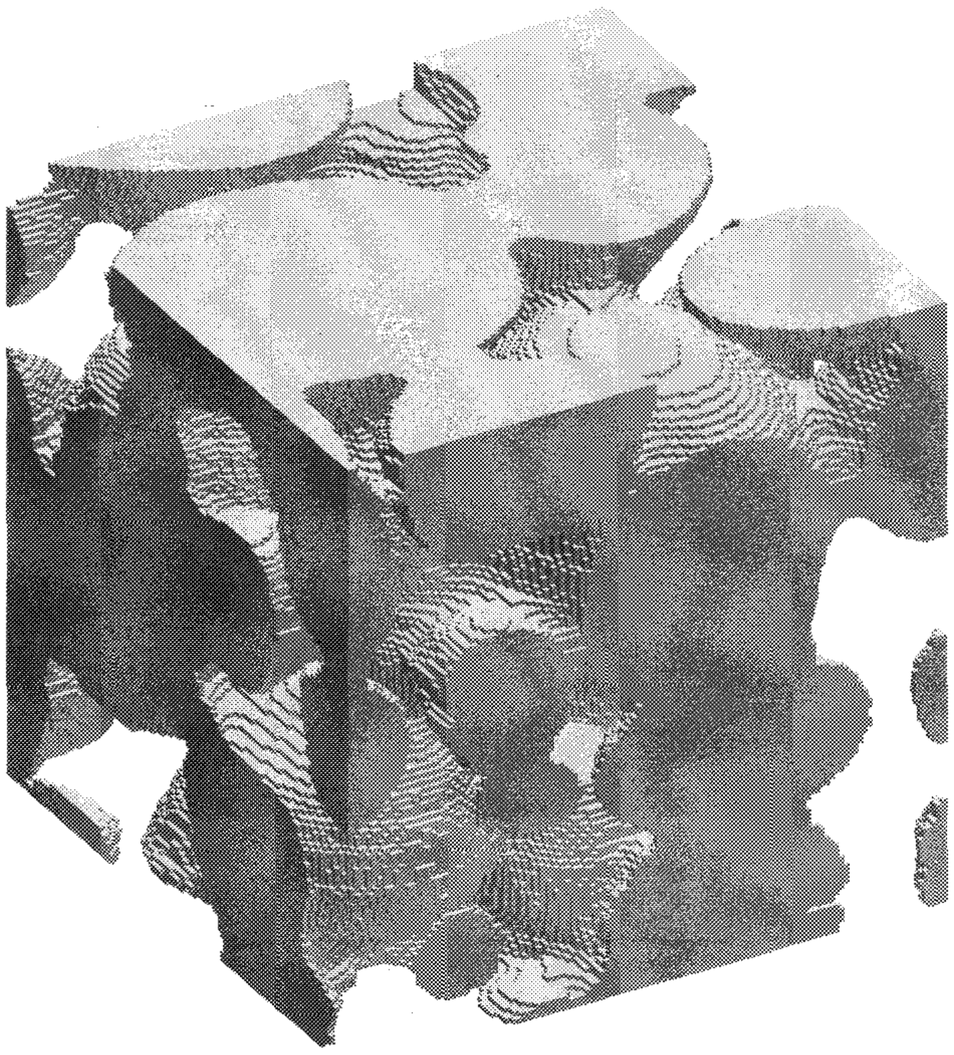

Fig. 6. 3D image reconstructed by manual contouring of the 64 section planes (sublimated sections). Resolution 128^3 voxels. Voxel size: 20 μm.

with an *isotropic* resolution of 20 μm. Each interpolated image was obtained by applying the XOR operator to the pair of neighbouring digitized section planes, then the pruned 2D skeleton [5] was computed on the result of the XOR operation. This pruned skeleton was taken as the contour of the intermediate image. We obtained a stack of 128 binary images containing 512×512 pixels whose resolution was dropped to 128×128 by assigning to each new pixel the closest integer (0 or 1) to the average value of the 16 previous corresponding pixels. Then the resolution became isotropic; Figure 6 presents the result.

2.4 Image processing

The above tedious contouring procedure was mostly automated in order to provide in a few hours a binary 128^3 voxel data file from a series of grey-level images of a serial cut. Both physical and numerical techniques were used. The respective features of manually and automatically contoured files will be compared later.

2.4.1 "Thermodynamic filtering"

This first stage took place in the cold laboratory, as described above about serial cuts. Experimentally, sample displacements between two successive views could not be prevented. Fortunately, only translations occurred.

2.4.2 Recentering of image pairs

From a given pair of images Im1 (fresh) and Im2 (sublimated), Im1 was recentered with respect to Im2 (the latter was used for manual contouring since it was most probably taken from a really motionless and mechanically stabilized sample). Im2 was successively translated from its original position by increments of 1 pixel, up to $\delta = 5$ pixels, on both sides of x and y axes, scanning a displacement field of 11×11 pixels. For each examined position of Im1, a difference image was built, defined by:

$$D_{\Delta i,\Delta j} = \left\{ \mathrm{Im1}_{\Delta i,\Delta j}(i,j) - \mathrm{Im2}(i,j) \right\}_{i,j=\delta}^{N-1-\delta},$$

where $\mathrm{Im}(i,j)$ denotes the grey level of the pixel of Im whose coordinates are i and j, N the resolution (here 128), and $(\Delta i, \Delta j)$ the current displacement. Figure 7a presents the result. The difference image D for which the sum of grey levels of all pixels was minimal has been chosen. For this one, the superposition of phtalate background patterns was considered optimal.

2.4.3 Difference image thresholding

D was thresholded to a binary image D_{bin} (visual control on a few image pairs of the collection) by using the grey-level histogram (see Fig. 7b). There remained mainly two sorts of defects in both black (pore) and white (grain) phases: small isolated patches and irregular parallel scratches.

2.4.4 Removal of small objects

All connected patches whose size was less than S_{min} pixels (this parameter was adjusted by visual control) were removed from both phases. For our sample, S_{min} was set to 5% of image size.

2.4.5 Removing of scratches

Most scratches were connected to grain edges; they were the visual result of sharpening defects of the microtome blade as observed under specularly reflected light. Those which were connected to grain edges were removed using a sort of "opening" procedure where the erosion stage (which broke thin connections) was followed by a removal of small objects as described above, then by a dilation to restore the size of remaining objects. The rate of both erosion and dilation was progressively increased until the relative variation of the number of grain pixels between two successive iterations is lower than a threshold value (5% in our case). The result is shown in Figure 7c.

The poor sharpness of our microtome blade also produced a fine-scale section unevenness which appeared under reflected light as many thin scratches. The size of isolated ones (not connected to grain edges) was then found to be lower than the size threshold S_{min}. Most of them were previously removed as "small objects".

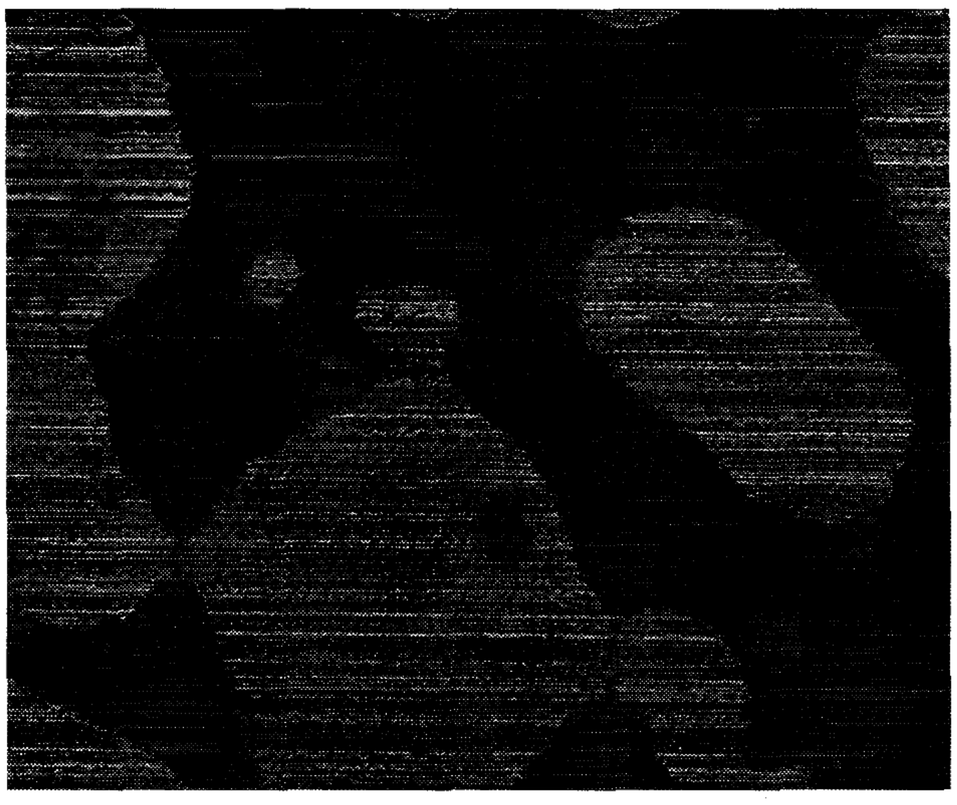

(a)

(b)

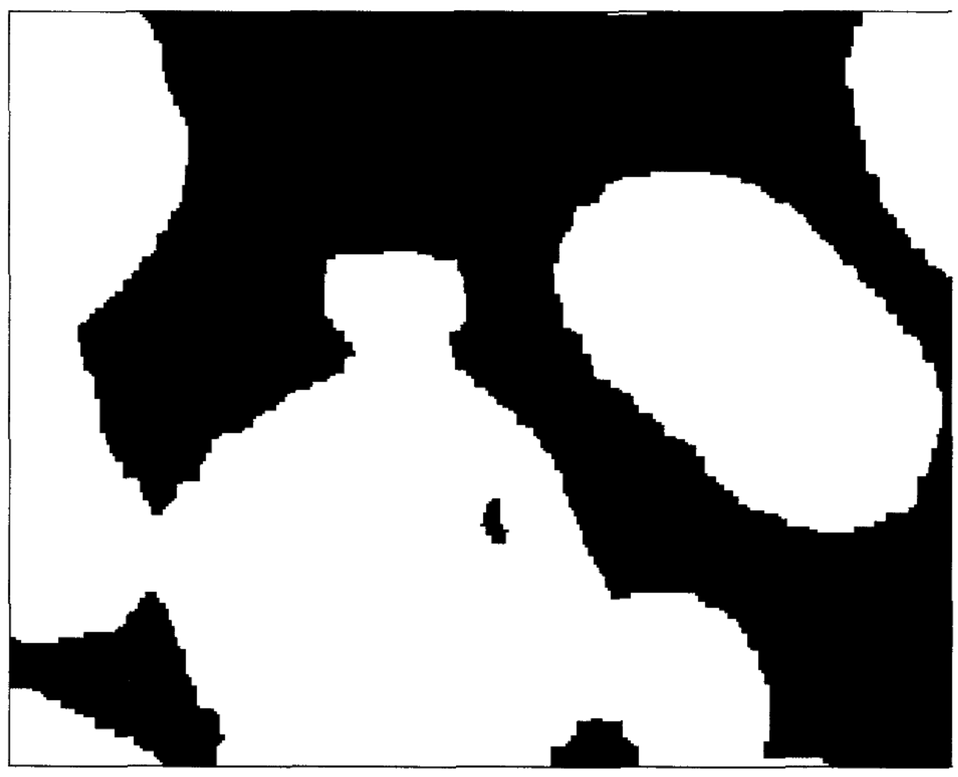

(c)

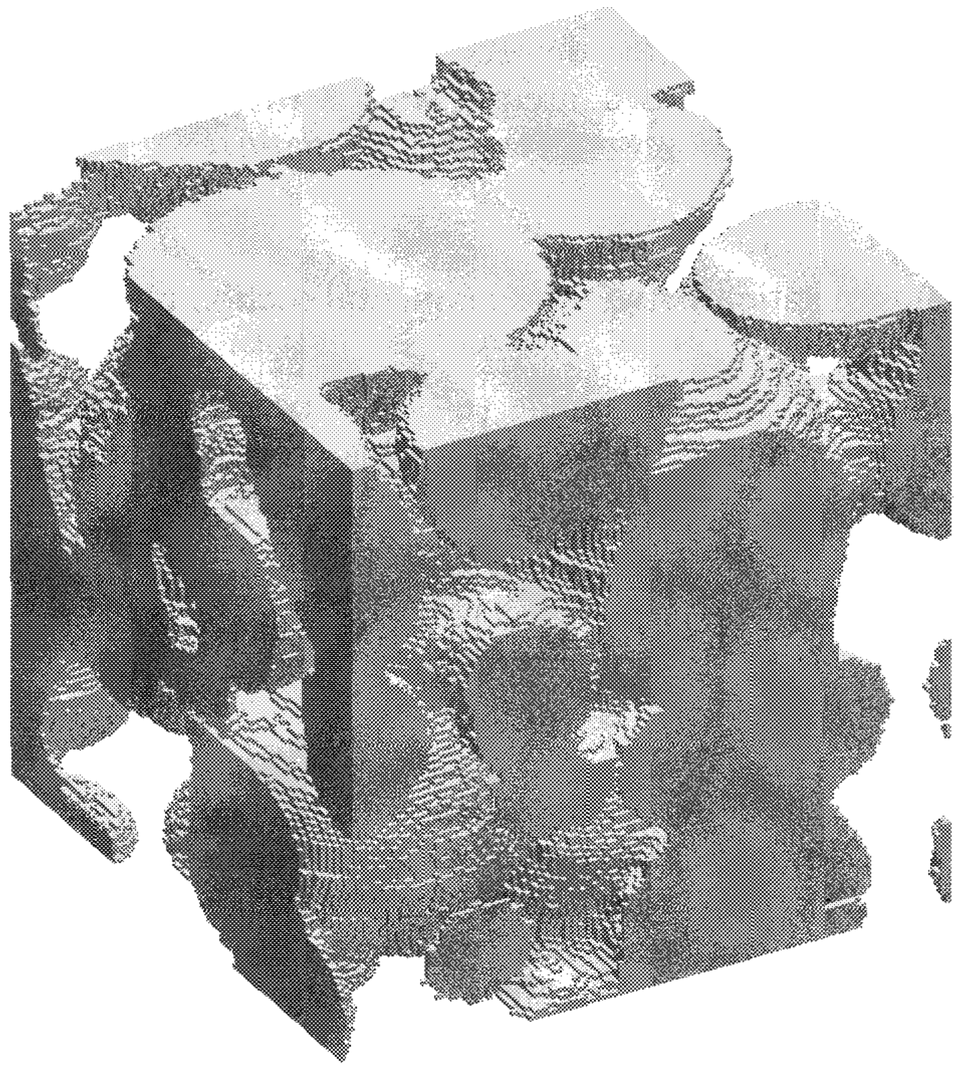

(d)

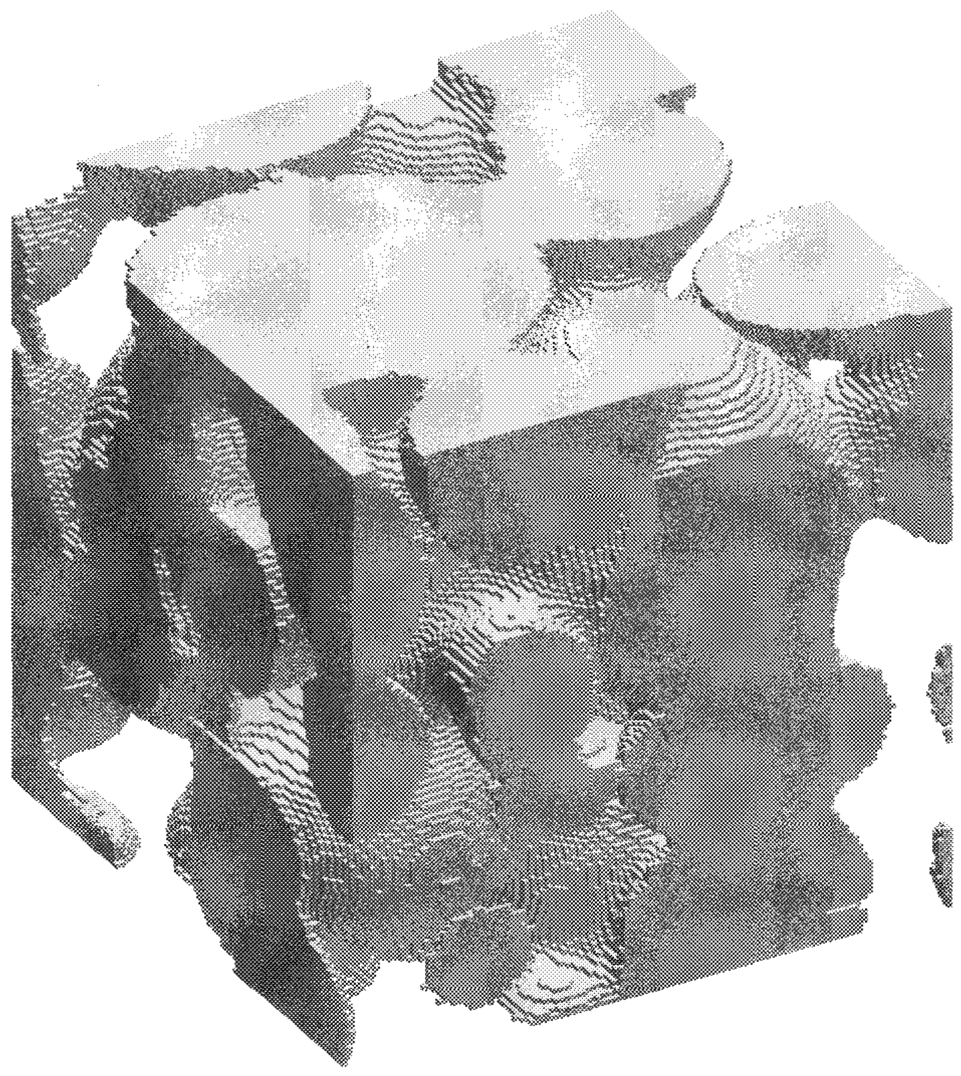

(e)

Fig. 7. Image processing of section planes. (a) Grey-level difference image D between fresh and sublimated section plane. (b) Thresholding of D using its grey level histogram. There remains mainly irregular parallel scratches. (c) Removal of scratches. (d) Raw 3D image, sampled at the desired resolution of 128^3 voxels. (e) Smoothed final 3D image.

2.4.6 "Final cleaning"

The very few remaining defects were generally clusters of scratches digitized as a unique wide scratch whose size exceeded $S_{\min}$. They were removed by hand.

2.4.7 Interpolation between experimental section planes

The average difference image $\langle D(k) \rangle$ between two successive planes k and $k+1$ was built; this grey-level image is defined by

$$\langle D(k) \rangle = \left\{ \frac{D(i,j,k) + D(i,j,k+1)}{2} \right\}_{\substack{i,j=0 \\ k=0}}^{\substack{N_{xy}-1 \\ N_z-1}}$$

where N_{xy} and N_z denote respectively xy resolution (512×512 in our case) and z resolution (here 64 section planes). $\langle D(k) \rangle$ was then thresholded at the grey level corresponding to the (statistical) median value of the grey-level histogram of $\langle D(k) \rangle$. The resulting "intermediate" B/W image D'_{bin} was then processed as previous "regular" images D'_{bin} (Sects. 2.4.4–2.4.6).

The binary (B/W) 3D data file at the desired N resolution (here 128) could then be generated (Fig. 7d).

2.4.8 3D smoothing

The above procedure did not account for continuity along the z axis. In particular, topological changes could not be "anticipated" in intermediate planes. This was achieved by applying 6 times a real-type averaging filter (kernel $[1.]^2_{i,j,k=0}$) to the data, then thresholding the resulting 256 grey level image at the value 128 in order to obtain the desired filtered B/W image. When applied to a cube, this filter rounded the edges into chamfers 3-voxel wide. The equivalent radius was less than 2 voxels, which is our lower threshold value for curvature computing. This level of smoothing was therefore consistent with our curvature model. Figure 7e shows the final result.

3 Validation

3.1 Choice of validation methods

The behavior of our curvature model has been tested on several objects including the experimental data file of refrozen wet snow. Three situations have been addressed:

- objects of known uniform curvature (sphere and zero-curvature analytic surface);
- object that presents sharp edges inside the image boundaries (cube);
- natural porous medium (snow sample).

For a geometric object of known curvature (like a sphere), the numerical values of curvature were simply compared to the analytic value. This was achieved by using the histogram of curvatures, that gave both bias and scattering of numerical values.

For other objects (such as experimental samples), the curvature map built from the grain medial axis (skeleton for short) can be compared for the same sample to the "complementary" map built from the pore skeleton. This validation is reliable because in 3D porous media, the connectivity properties of grain and pore phases are not related together. For instance, breaking a narrow bridge between two grains does not change the ability to connect neighboring pores. The calculations have been performed on the same set of voxels – that is – the first layer of grain's phase voxels (whose background distance with regard to grains is 1, 4/3 or 5/3). Therefore, the evaluation of curvature using the grain skeleton can be considered independent of the evaluation using the pore skeleton. For each object, the two corresponding curvatures have been superimposed, and the scattering graph of curvatures has been drawn. Each dot of the scattering graph corresponds to a given voxel of the object's surface Σ. Its curvature value computed from the pore phase ("complementary image") skeleton is plotted *versus* the value computed from the grain phase ("image") skeleton. Each voxel of Σ for which both values of curvature are available is represented on the graph.

Finally, for the snow sample, the histograms of 3D and 2D curvatures (the latter on *outlines* of grain clusters) were compared. For wet snow, grains assume a quasi-spherical form: therefore, the curvature of convex parts of outlines should be close to 3D values on (convex) grains. Naturally, visual examination of generated curvature maps was a subjective but powerful means of debugging and validation because it allowed the locating of defects on the object.

3.2 Results for geometric shapes

The model has been run on three test files, each of 128^3 voxels. As discussed later, curvature was not computed on voxels whose distance to image edges was less than 8 voxels. The effectively processed volume was then 112^3 voxels.

3.2.1 Sphere of radius R = 50 voxels

Owing to its complete uniformity ($R_1 = R_2 = R$), the sphere was a good check of bias and scattering of numerical data. From Figure 8c, the histograms of image ("inner" skeleton: the center of the sphere) and complementary ("outer" skeleton) merge and no bias can be seen: the peak is at $C = 0.02 = 1/R$. On the scattering graph, the circular shape of the dot pattern shows that:

- the spherical shape is respected: no elongation is "seen" in any direction;
- point scattering is isotropic.

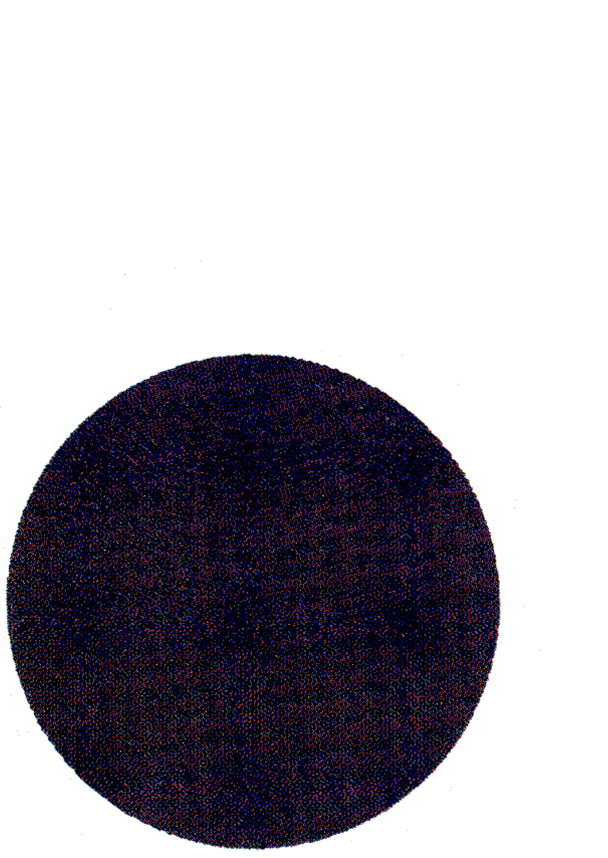

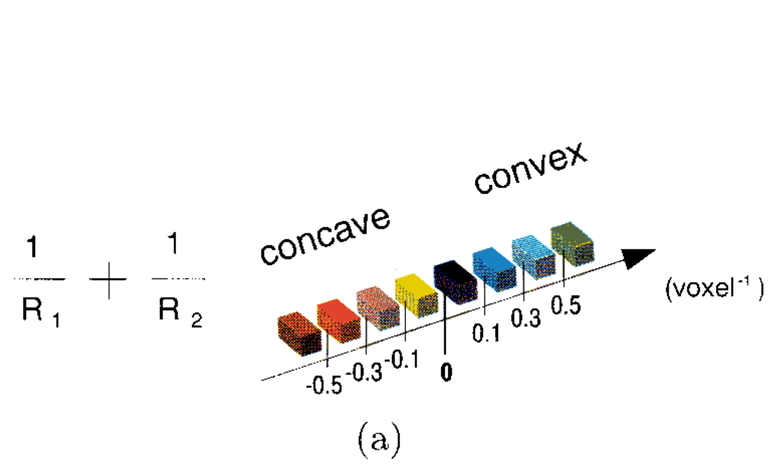

(a)

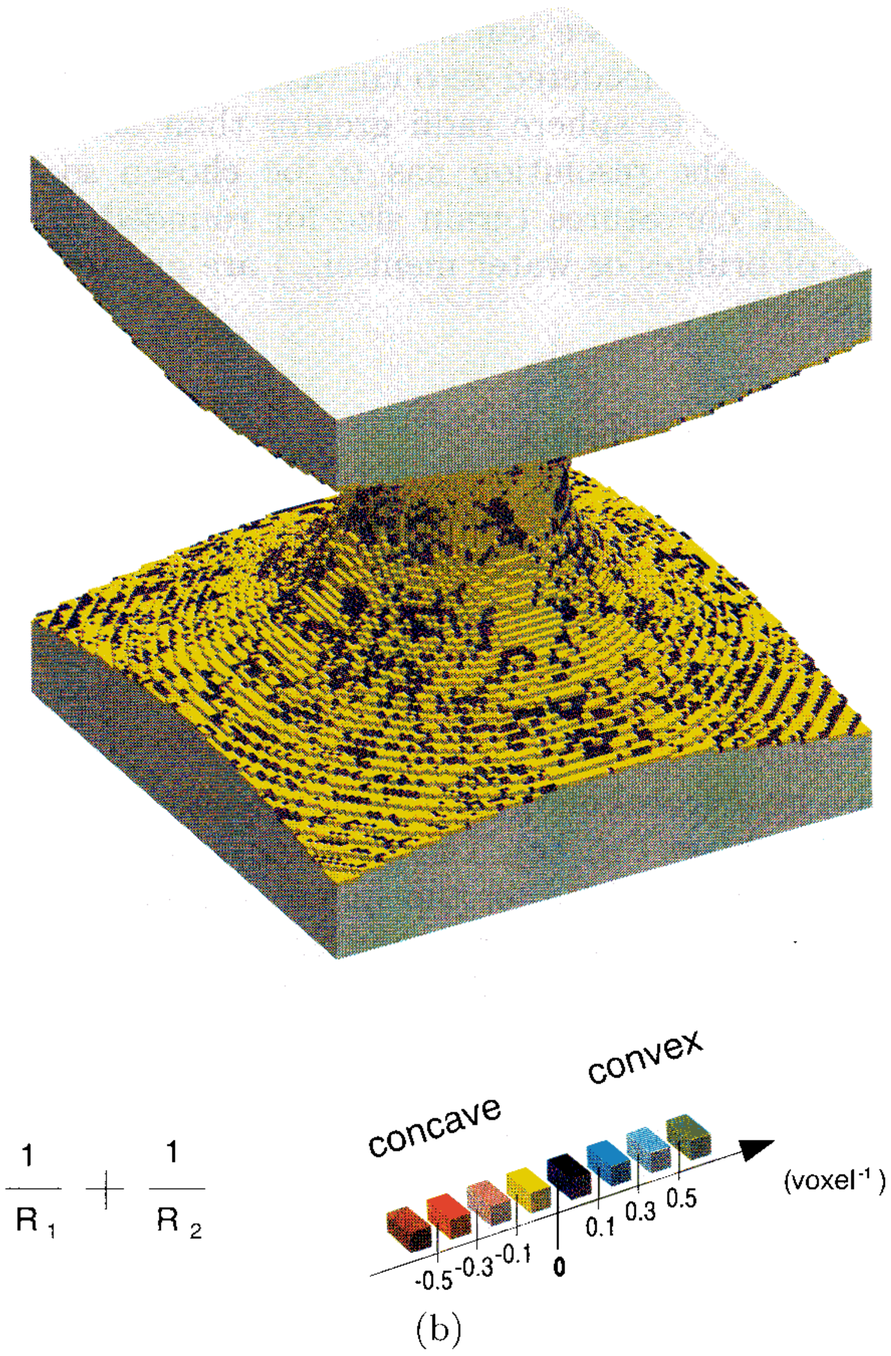

(b)

curvature histograms

scattering graph

surfaces of known curvature

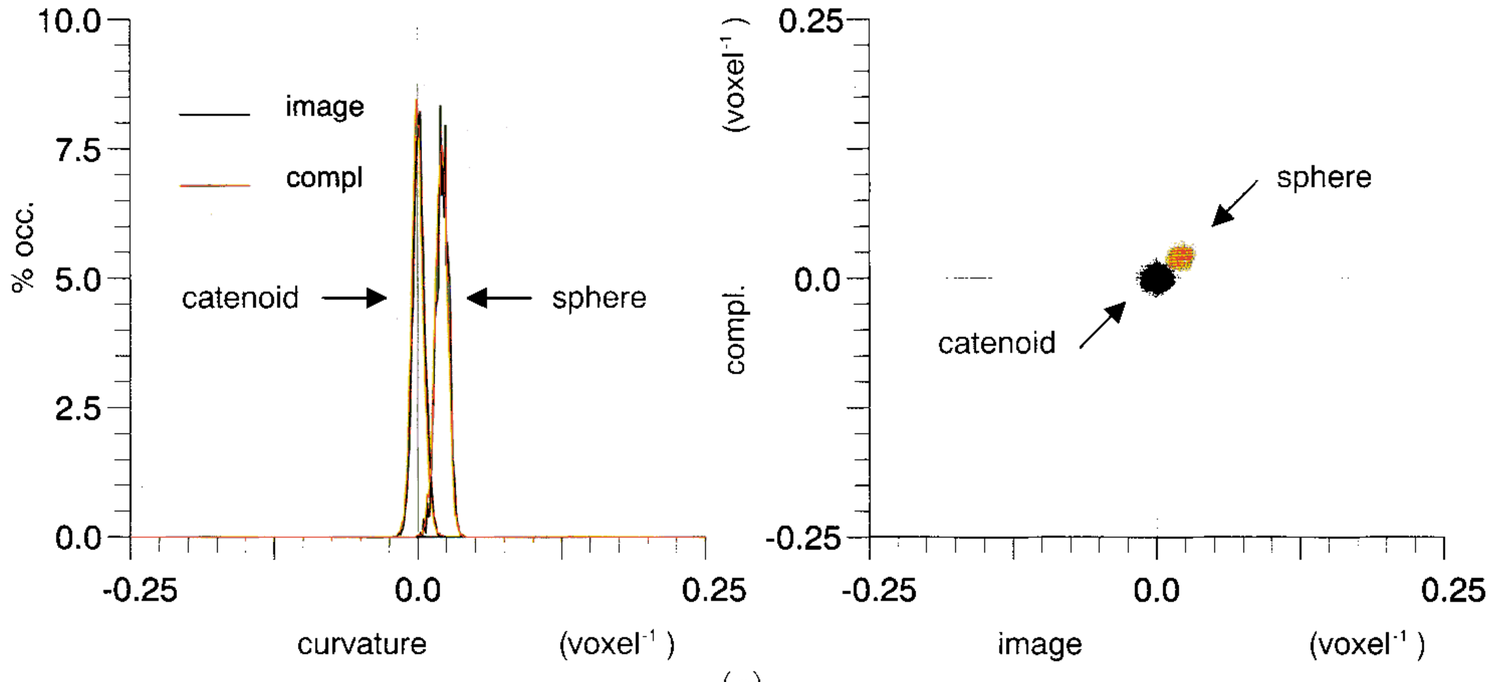

(c)

Fig. 8. Results on simple geometric shapes. (a) *Euclidean sphere of radius 50 voxels.* The color scale at the bottom gives the computed values of curvature $C = (1/2)(1/R_1 + 1/R_2)$ expressed in voxel^{-1}. (b) *Zero-curvature analytic surface (catenoid) of equation:* $\sqrt{(x-64)^2 + (y-64)^2} = 20\cosh((z-64)/20)$. (c) *Curvature statistics.* Histograms were computed using 1000 class. The occurrence percentage %occ plotted on the y axis is defined as $\dfrac{\text{nb. voxels in a given class}}{\text{nb. voxels on whole object surface}}$. For each object, histograms built from image and complementary skeletons merge almost exactly, and peak at the analytic value of C for both shapes. Similarly, the symmetry of dot patterns on the scattering graph suggests a good isotropy of computations.

Examining the width of the histogram (complete half-width 0.02 voxel^{-1}), we can see that values lower than 0.02 voxel^{-1} are considered zero curvatures; for instance, this corresponds to sphere radii greater than 50 voxels. Consequently, the resolution has to be chosen so that all significant curvatures (grain size for rounded grains, curvature of bridges or water menisci...) are greater than 0.02 voxel^{-1}.

3.2.2 Zero curvature surface

The program was applied to an analytic zero-curvature surface, a catenoid (the shape assumed by a soap film between two rings) with equation:

$$\sqrt{(x-64)^2+(y-64)^2} = 20\cosh\left(\frac{z-64}{20}\right).$$

Curvature histograms merge too, with a peak exactly centered at $C = 0$ (see Fig. 8c). The peak width remains similar to the value obtained for the sphere; the same agreement is observed for the scattering graph. It should be noted that these results are obtained "without" the 8 first layers of voxels. Closer to the edges of the image, the two histograms shift together and the dot pattern in the scattering graph widens dramatically. We suppose that this limit of 8 voxels comes from the conditions of computation of R_1 and R_2 in 2D. The longest arc that can be used for radius calculation was set to 17 pixels, 8 on each side plus the current point. In the program, the edge of the image is processed in the same way as the edge of the object. Systematic errors occur even for a skeleton ending at a normal to an image edge. For this reason, 3D curvature was not computed on the 8 first layers of voxels.

3.2.3 Cube

For a polyhedron, curvature is zero on facets and infinity on edges and corners. The cube provided a useful check of the effects of sharp edges on computations. It has been tilted with regard to coordinate axes to avoid additional artifacts (most improbable in reality) due to a rigorous alignment of the object's surface and field boundaries. In the convex region, *i.e.* close to cube edges, discrepancies can be seen in both the histogram comparison (between 0.05 and 0.15 voxel^{-1}) and scattering graph (in the form of a wide "plume"). It can be seen from Figure 9a that these numerical errors are mostly limited to the six first voxel rows adjacent to cube edges. Field boundaries present also (undesired) sharp edges. This is the reason for the limit of 8 voxels distance from field boundaries (two more voxels to ensure that side effects are suppressed) introduced in Section 3.2.

3.3 Natural snow

3.3.1 Results in 3D

For this sample of rounded grains (quasi-spherical), we expected uniform positive (convex) curvatures for grains. Since water wets ice and because of capillarity, all water menisci should be connected together and curvature should be negative or zero in any part of menisci. Moreover, at the end of the drainage stage, when the sample is still at $T = T_d = 0$ °C, the capillary pressure should be uniformly negative. The variation of hydrostatic pressure due to the height of the sample (2.5 mm) is negligible as compared to capillary pressure around millimeter-size grains. Small rearrangements of menisci curvature might occur because of the slow refreezing of the sample, but a characteristic (negative) value is expected in such regions.

The result of Figure 10a fulfills these statements, as can be seen from the layout of colors. In the same way, curvature histograms present a characteristic bulge in negative values, which can be located at -0.075 voxel^{-1}. Voxel size being $a = 2 \times 10^{-5}$ and water surface tension being $\gamma_{LV} = 0.073$ N/m, the corresponding capillary pressure is $P_c = 2C\gamma_{LV}/a \approx 550$ Pa. In hydrostatic conditions, the corresponding height of the sample above the water saturated layer would be about 5 cm at the moment of sampling. This value of a few cm is consistent with our sampling conditions (snow block height $\sim$ 20 cm). Moreover, the two histograms (from inner and outer skeleton) merge almost exactly (see Fig. 10b). They are also in excellent agreement with results obtained from the manually contoured image of the snow sample (Fig. 6); this provides a reliable validation of the partly automatic generation of the 3D data file presented above.

3.3.2 Comparison with 2D results

The (2D) histogram of *outline* curvatures has been superimposed to 3D histograms in Figure 10b. As discussed above, a reasonable comparison between 2D and 3D histograms can be done only for rounded shapes (such as wet grains), in the regions of positive curvatures; concave regions are hidden in most cases. The 2D histogram has then been normalized with respect to the number of positive values. The three histograms peak at the same value of 0.07 voxel^{-1} – that is – a mean grain radius of 0.57 mm.

Whereas concave regions can hardly be detected in 2D, 2D positive values fit correctly 3D histograms. This is consistent with the quasi spherical shape of grains in our sample (the arc which generates the outline is included in a plane that contains the normal $\mathbf{n}$).

3.4 Discussion of resolution vs. field practical limits

Computing local curvature on a voxel P uses a given number of neighboring voxels (in our examples, a 20^3 cube around P). The range of correctly evaluated curvature values is related to the neighbouring size, and this relationship is not straightforward. The problem has been addressed in 2D [8] for the most common grain shapes and convex (positive) curvatures. For instance, a neighbouring size of 17 pixels allows correct rendering of radii between 0.125 and 0.75 mm for a scaling factor of 15 μm per pixel

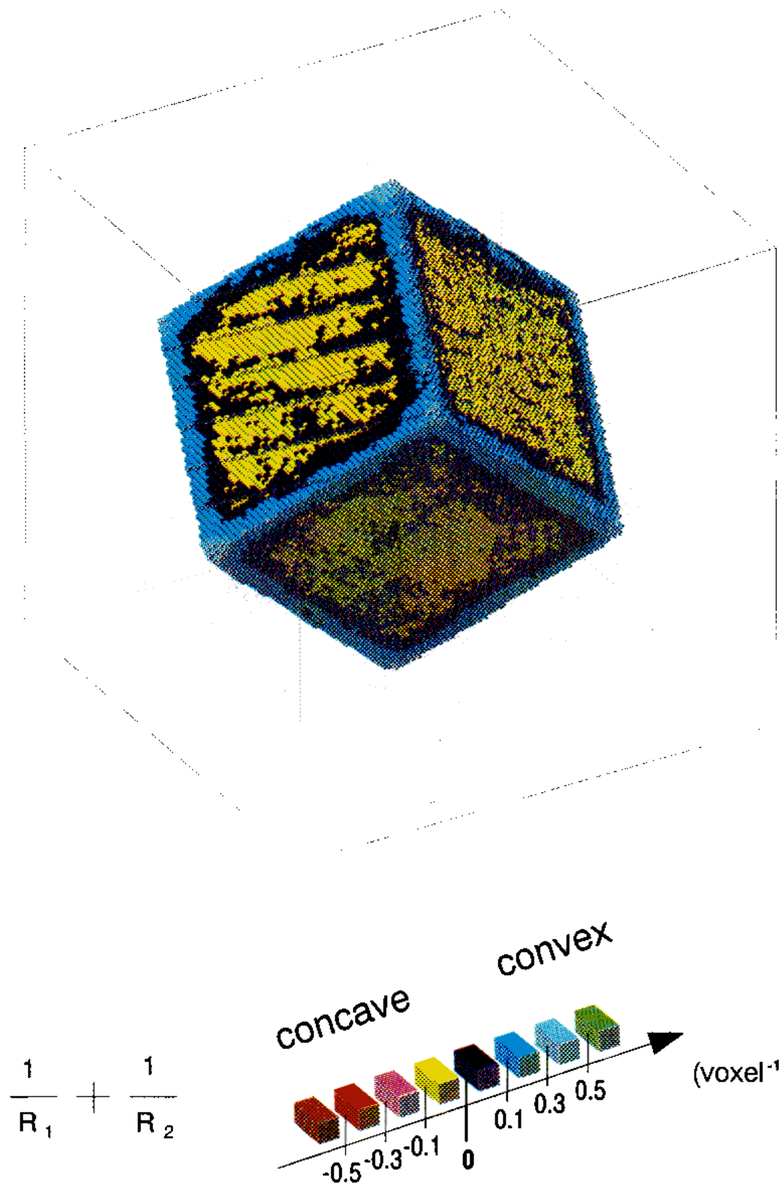

(a)

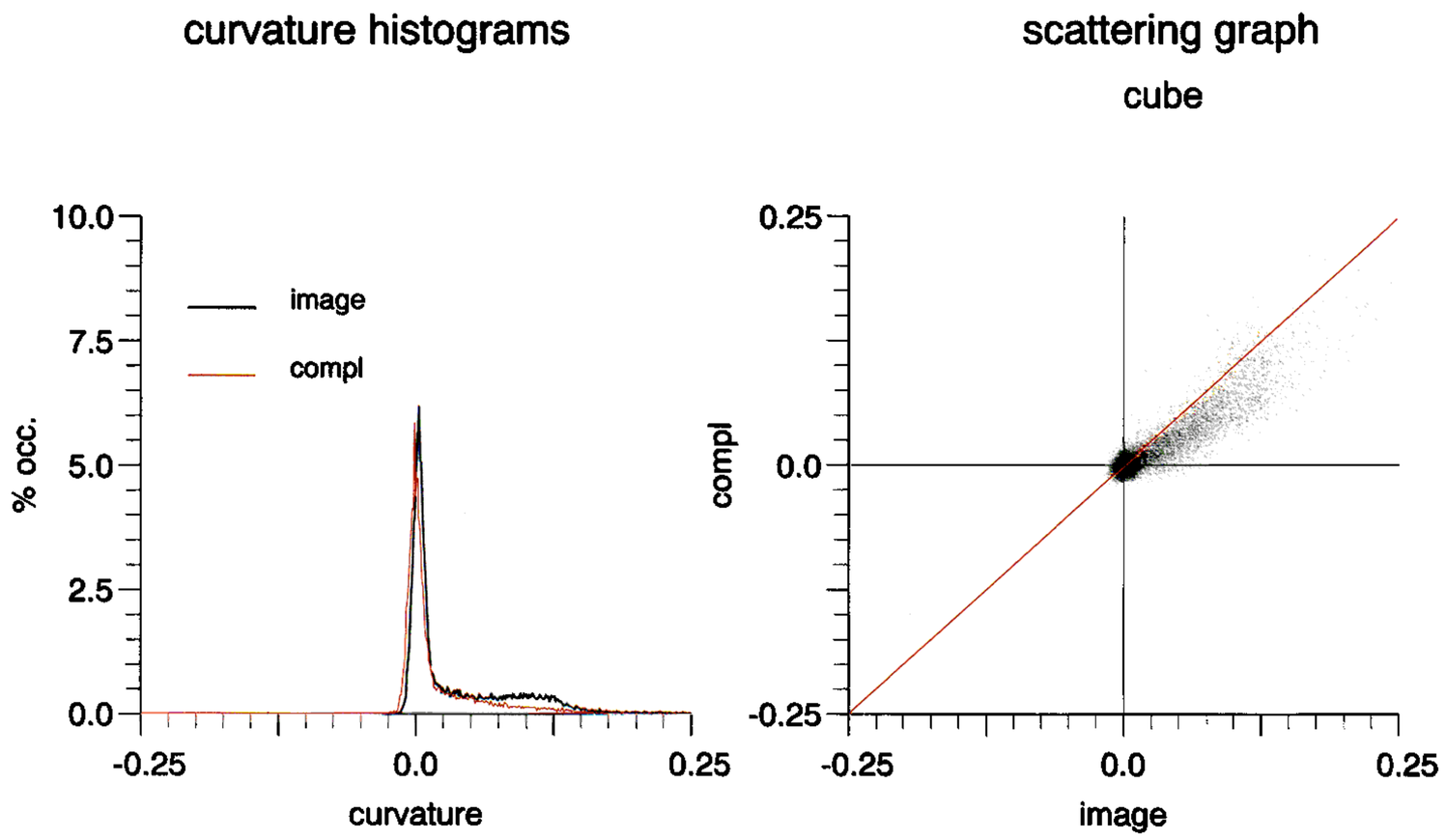

(b)

Fig. 9. Behaviour of the model in difficult conditions: cube tilted with regard to coordinate axes. (a) *Curvature map.* The effects of a steep edge are limited to the 8 neighbouring voxels. The smoothing procedure described in Section 2.4.8, which affects only the 2 neighbouring voxels, is therefore consistent with the intrinsic side effects of the model. (b) *Statistics.* Defects appear in the convex part of histograms (close to the edge); a divergence between histograms can be seen in the 0.08–0.012 voxel^{-1} region. On the scattering graph, errors appear as a "plume", tilted with regard to the bisector, at the right of the central spot of zero curvature facets (correctly computed). This tilt and the divergence between histograms show that to minimize errors (and increase net accuracy), curvature computations on convex edges should be performed using the complementary skeleton and *vice versa.*

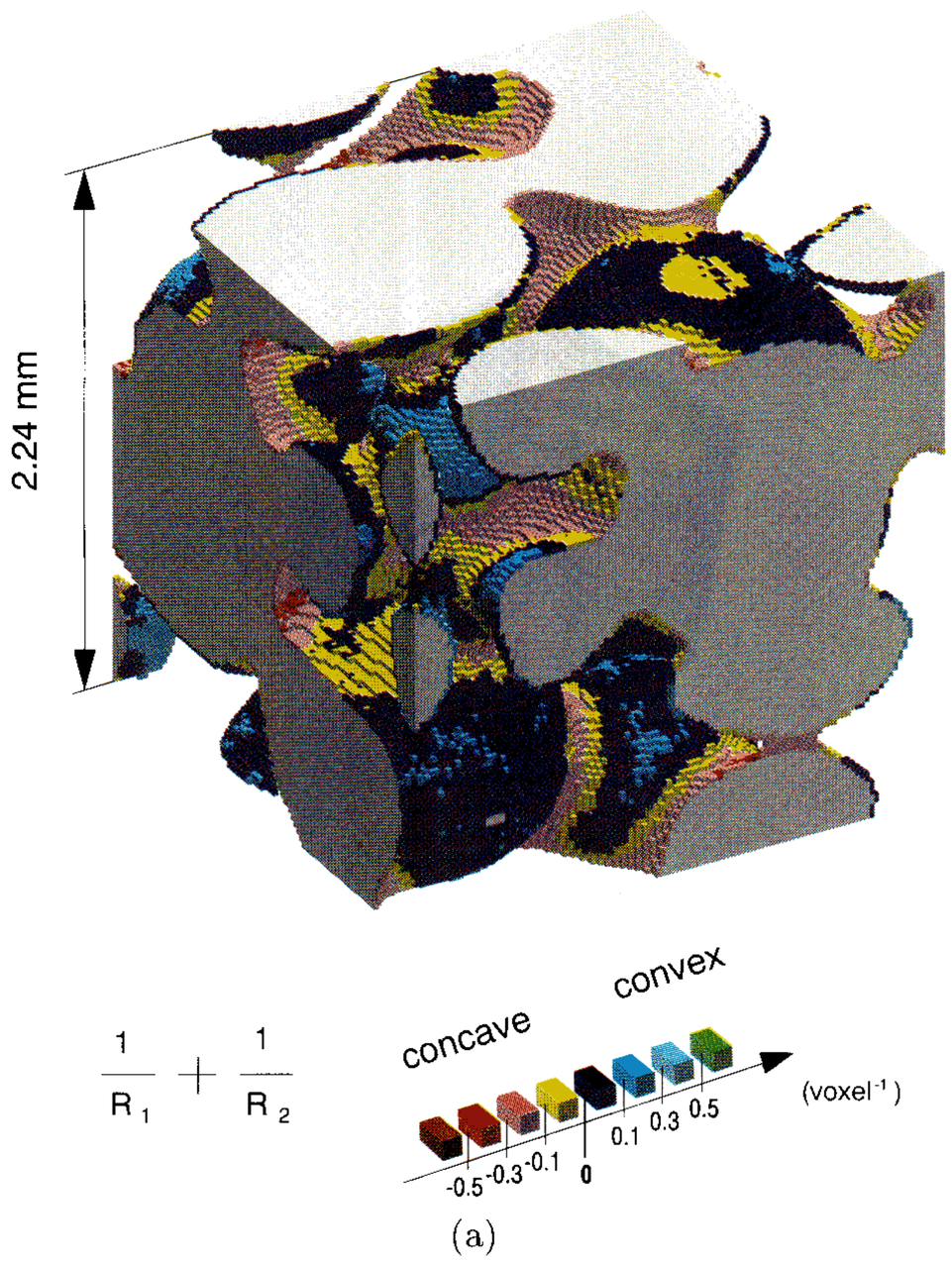

Fig. 10. Real wet snow sample. (a) *Curvature map.* Most of the concave regions appear in pink (on bottom color scale, $-0.15 < C \leq -0.05$ voxel^{-1}), and the layout of these regions suggest clearly the path of (previous) water menisci. These curvature values correspond to a capillary depression of ∼550 Pa (see text), consistent with the conditions of sample preparation. (b) *Statistics.* In the concave part of the histograms, a bulge can be seen around -0.15 voxel^{-1}. Image (black) and complementary (red) histograms merge, and on the scattering graph, the dot pattern follows the bisector. The 2D histogram of grain outlines of the same sample (green) fits correctly 3D histograms on its convex part. Where they have sense, 2D and 3D curvatures are in good agreement.

(comparable to our 3D voxel size of 20 μm), all radii (concave and convex) fall within these limits on 2D sections of the experimental sample. Moreover, we know from the experience of digitizing snow samples that in the case of wet grains, it is necessary to analyze only a few grains (generally 2 or 3) to obtain values of convex radii that are relevant to the whole sample. This is consistent with the fact that the standard deviation of convex curvatures is low for wet grains [8]. On our 2D sections the summed length (in pixels) of grain perimeters was found to be equal to about 5 times the mean perimeter of one grain (there are about 5 grains per section plane). Since the actual curvature computation is two-dimensional (in one given section plane $\Pi_1(P)$ or $\Pi_2(P)$), we can conclude that the neighboring size of 20^3 voxels in 3D is convenient for computing curvatures on our wet snow sample. However, this value has to be considered again for computation on other types of grains. Moreover, as shown in Figure 10b, the convex part of 2D histograms fits accurately 3D curvatures; this provides an additional hint of a good agreement between resolution and field size for the considered sample.

On the other hand, a correct assessment of low curvatures requires a large number of pixels. For instance, Figure 8a shows that the model cannot account for objects "smoother" than a sphere of radius 50 voxels using our parameter settings; such objects are considered as zero curvature surfaces. This is not a problem in the capillary regime since the thermodynamic contribution of very low curvatures is negligible.

Outlook and conclusion

This work aims at providing a database of characteristic three-dimensional snow microstructures adapted to the fine-scale description of capillarity, percolation in the *unsaturated* regime (by far the most frequent with snow) and snow metamorphism. The two following subjects have been addressed in this study.

3D imaging

Serial cuts have been applied to snow samples for over 10 years [12]. By using specularly reflected light in our experiments, we could prevent problems due to the numerous and various optical "defects" of snow, which is neither opaque nor fully transparent. Combined with standard morphologic image processing, the use for each section plane of views from both fresh and sublimated material allowed a reliable and quasi-automatic contouring of the ice phase; this procedure led to a binary 3D data file in a reasonable time for unique acquisition (a few hours for 128^3 voxel).

However, building a database with such long and delicate experiments in a cold laboratory would be tedious. Modern imaging techniques such as NMR microscopy [13] and X-ray tomography [14] allow 3D reconstruction of porous media with a resolution better than 20 μm. In fact, our serial cut experiment has to be considered as a necessary means of direct validation of the above modern imaging techniques on snow. Active collaborations are now in progress, with Université Paris XI (U2R2M, Orsay) on NMR microscopy, and with ESRF synchrotron (Grenoble) on X-ray tomography [15], and we expect the first results in the next few months.

Curvature modeling

After validation on geometric shapes, the curvature model has been successfully tested on our 3D image of real snow. Although connection properties of the two phases are unrelated, the histogram of curvatures remains unchanged whether curvatures are computed from grain phase ("image") or from pore phase ("complementary"). A curvature model is a valuable tool for the study of real porous media. In the field of snow physics, one possible application is to locate on refrozen wet snow the percolation paths which were active before sampling: a realistic modeling of water percolation, including tortuosity, will become possible. Another use of this model for snow would be to allow a fully physical parameterization of grain metamorphism in snowcover evolution models such as Crocus [16].

We thank J.P. Laurent and P.M. Adler for fruitful discussions and providing us valuable test files, and P. Lamboley who wrote the program for visualizing 3D data files.

References

1. F.A.L. Dullien, *Porous media; fluid transport and pore structure* (Academic Press, 1979).
2. S.C. Colbeck, A review of sintering in seasonal snow, CRREL Report 97-10, 1998.
3. A.W. Adamson, *Physical chemistry of surfaces*, 5th edn. (Wiley, New York, 1990).
4. J.M. Chassery, A. Montanvert, *Géométrie discrète en analyse d'images* (Hermès, Paris, 1992).
5. J. Serra, *Image analysis and mathematical morphology* (Academic Press, 1982), Vol. 1.
6. G. Borgefors, Comp. Vis. Graph. Image Proc. **27**, 321 (1984).
7. F. Rolland, Ph.D. thesis, University Joseph Fourier, Grenoble, 1991.
8. B. Lesaffre, E. Pougatch, E. Martin, Ann. Glaciol. **26**, 112 (1998).
9. J.B. Brzoska, C. Coléou, B. Lesaffre, J. Glaciol. **44**, 54 (1998).
10. H.S. Boyne, D.J. Fisk, A laboratory comparison of field techniques for measurement of the liquid water fraction of snow, Special CRREL Report 90-3, 1990.
11. E. Brun, E. Pahaut, J. Glaciol. **37**, 420 (1991).
12. W. Good. Thin sections, serial cuts and 3D analysis of snow, Publ. No. 192 IAHS, *Proc. Symp. Avalanche formation, movement and effects*, Davos, pp. 35-48.
13. P. Callaghan, *Principles of Magnetic Resonance Microscopy* (Oxford, University Press, 1991).
14. P. Cloetens, M. Pateyron-Salomé, J.Y. Buffière, G. Peix, J. Baruchel, F. Peyrin, M. Schlenker, J. Appl. Phys. **81**, 5878 (1997).
15. J.B. Brzoska, C. Coléou, B. Lesaffre, S. Borel, O. Brissaud, W. Ludwig, E. Boller, J. Baruchel, ESRF Newsletters (in press).
16. E. Brun, P. David, M. Sudul, G. Brunot, J. Glaciol. **38**, 13 (1992).